

chronic pain-induced synaptic changes are global, affecting all excitatory inputs onto MSNs, or rather are input-specific.

Previous studies on mouse models of chronic pain report no change in home cage behaviors or measures of affective behaviors during the first month of the pathology (14, 15). Within a similar time frame, by focusing on a more subtle aspect of goal-directed operant behavior—the motivation to work for natural reward—we found that motivation was impaired. Our results suggest that pain-induced synaptic adaptations within the NAc contribute to a subjective impairment in the ability to initiate or sustain physical or mental tasks (47, 48), or to the symptom of central fatigue commonly reported by chronic pain patients (1, 2). These results also suggest specific synaptic targets that may be susceptible to therapeutic interventions.

REFERENCE AND NOTES

1. B. Nicholson, S. Verma, *Pain Med.* **5**, S9–S27 (2004).
2. D. C. Turk, J. Audette, R. M. Levy, S. C. Mackey, S. Stanos, *Mayo Clin. Proc.* **85**, S42–S50 (2010).
3. J. Dershi, P. B. Polatin, R. J. Gatchel, *Psychosom. Med.* **64**, 773–786 (2002).
4. T. Jonsson et al., *Acta Anaesthesiol. Scand.* **55**, 69–74 (2011).
5. J. P. Johansen, H. L. Fields, B. H. Manning, *Proc. Natl. Acad. Sci. U.S.A.* **98**, 8077–8082 (2001).
6. D. Borsook et al., *Eur. J. Pain* **11**, 7–20 (2007).
7. C. A. von Hehn, R. Baron, C. J. Woolf, *Neuron* **73**, 638–652 (2012).
8. A. I. Basbaum, D. M. Bautista, G. Scherrer, D. Julius, *Cell* **139**, 267–284 (2009).
9. J. D. Salamone, M. Correa, *Neuron* **76**, 470–485 (2012).
10. G. J. Mogenson, D. L. Jones, C. Y. Yim, *Prog. Neurobiol.* **14**, 69–97 (1980).
11. B. W. Balleine, J. P. O'Doherty, *Neuropsychopharmacology* **35**, 48–69 (2010).
12. D. J. Scott, M. M. Heitzeg, R. A. Koeppe, C. S. Stohler, J.-K. Zubieta, *J. Neurosci.* **26**, 10789–10795 (2006).
13. M. N. Baliki et al., *Nat. Neurosci.* **15**, 1117–1119 (2012).
14. R. Urban, G. Scherrer, E. H. Goulding, L. H. Tecott, A. I. Basbaum, *Pain* **152**, 990–1000 (2011).
15. I. Yalcin et al., *Biol. Psychiatry* **70**, 946–953 (2011).
16. H. S. Roane, *J. Appl. Behav. Anal.* **41**, 155–161 (2008).
17. C. P. O'Brien, E. L. Gardner, *Pharmacol. Ther.* **108**, 18–58 (2005).
18. J. A. Shuen, M. Chen, B. Gloss, N. Calakos, *J. Neurosci.* **28**, 2681–2685 (2008).
19. A. Sanz-Clemente, R. A. Nicoll, K. W. Roche, *Neuroscientist* **19**, 62–75 (2013).
20. B. R. Lee, Y. Dong, *Neuropharmacology* **61**, 1060–1069 (2011).
21. M. B. Max et al., *Mol. Pain* **2**, 14 (2006).
22. P. G. Unschuld et al., *J. Affect. Disord.* **105**, 177–184 (2008).
23. N. R. Wray et al., *Mol. Psychiatry* **17**, 36–48 (2012).
24. Y. S. Nikolova, E. K. Singhi, E. M. Drabant, A. R. Hariri, *Genes Brain Behav.* **12**, 516–524 (2013).
25. M. E. Anderson, J. Runesson, I. Saar, U. Langel, J. K. Robinson, *Behav. Brain Res.* **239**, 90–93 (2013).
26. V. Sergeev, C. Broberger, T. Hökfelt, *Brain Res. Mol. Brain Res.* **90**, 93–100 (2001).
27. H. Imbe et al., *Neurosci. Lett.* **368**, 102–106 (2004).
28. H. Nishii, M. Nomura, H. Aono, N. Fujimoto, T. Matsumoto, *Regul. Pept.* **141**, 105–112 (2007).
29. X.-L. Gu, Y.-G. Sun, L.-C. Yu, *Behav. Brain Res.* **179**, 331–335 (2007).
30. B. K. Lim, K. W. Huang, B. A. Grueter, P. E. Rothwell, R. C. Malenka, *Nature* **487**, 183–189 (2012).
31. Y. Dong, J. P. Tyszkiewicz, T. M. Fong, *J. Neurophysiol.* **95**, 3228–3234 (2006).
32. E. B. Einstein, Y. Asaka, M. F. Yeckel, M. J. Higley, M. R. Picciotto, *Eur. J. Neurosci.* **37**, 1541–1549 (2013).
33. E. J. Cobos et al., *Pain* **153**, 876–884 (2012).
34. K. Yashiro, B. D. Philpot, *Neuropharmacology* **55**, 1081–1094 (2008).
35. P. F. Dureux et al., *Nat. Neurosci.* **12**, 393–395 (2009).
36. S. Jurado, V. Biou, R. C. Malenka, *Nat. Neurosci.* **13**, 1053–1055 (2010).
37. S. M. Nicola, *J. Neurosci.* **30**, 16585–16600 (2010).
38. A. M. Farrar et al., *Neuroscience* **166**, 1056–1067 (2010).
39. J. L. Santerre et al., *Pharmacol. Biochem. Behav.* **102**, 477–487 (2012).
40. M. K. Lobo, E. J. Nestler, *Front. Neuroanat.* **5**, 41 (2011).
41. J. C. Lemos et al., *Nature* **490**, 402–406 (2012).
42. B. B. Land et al., *J. Neurosci.* **28**, 407–414 (2008).
43. G. Dölen, A. Darvishzadeh, K. W. Huang, R. C. Malenka, *Nature* **501**, 179–184 (2013).
44. M. Marinelli, P. V. Piazza, *Eur. J. Neurosci.* **16**, 387–394 (2002).
45. G. Cui et al., *Nature* **494**, 238–242 (2013).
46. F. Kasanetz et al., *Science* **328**, 1709–1712 (2010).
47. A. Chaudhuri, P. O. Behan, *Lancet* **363**, 978–988 (2004).
48. K. B. Norheim, G. Jonsson, R. Omdal, *Rheumatology (Oxford)* **50**, 1009–1018 (2011).

ACKNOWLEDGMENTS

We thank members of the Malenka lab for helpful feedback and comments during the study. We thank S. Fang and A. Darvishzadeh for help with stereotaxic injections and P. Rothwell for setting up the operant behavior chambers and software. This work was supported by a Banting postdoctoral fellowship (N.S.) and the NIH (R.C.M.). All primary data (behavioral, electrophysiological, and immunohistochemical) are archived in the Department of Psychiatry and Behavioral Sciences, Stanford University School of Medicine.

SUPPLEMENTARY MATERIALS

www.sciencemag.org/content/345/6196/535/suppl/DC1
Materials and Methods

Figs. S1 to S10
References (49–54)

27 March 2014; accepted 12 June 2014
10.1126/science.1253994

REPORTS

PHOTOVOLTAICS

Interface engineering of highly efficient perovskite solar cells

Huanping Zhou,^{1,2*} Qi Chen,^{1,2*} Gang Li,¹ Song Luo,^{1,2} Tze-bing Song,^{1,2} Hsin-Sheng Duan,^{1,2} Ziruo Hong,¹ Jingbi You,¹ Yongsheng Liu,^{1,2} Yang Yang^{1,2,†}

Advancing perovskite solar cell technologies toward their theoretical power conversion efficiency (PCE) requires delicate control over the carrier dynamics throughout the entire device. By controlling the formation of the perovskite layer and careful choices of other materials, we suppressed carrier recombination in the absorber, facilitated carrier injection into the carrier transport layers, and maintained good carrier extraction at the electrodes. When measured via reverse bias scan, cell PCE is typically boosted to 16.6% on average, with the highest efficiency of ~19.3% in a planar geometry without antireflective coating. The fabrication of our perovskite solar cells was conducted in air and from solution at low temperatures, which should simplify manufacturing of large-area perovskite devices that are inexpensive and perform at high levels.

Organic-inorganic hybrid materials, particularly the perovskite family, have shown great promise for use in field-effect transistors, light-emitting diodes, sensors, and photodetectors for more than a decade (1). Recently, the power conversion efficiency (PCE)

of lead halide perovskite (CH₃NH₃PbX₃, X = Cl, Br, I)-based thin film photovoltaic devices has skyrocketed from 3.8% to more than 17% in just 4 years (2–6). In a typical perovskite solar cell, a several-hundred-nanometer-thick absorber layer, either with or without mesoporous scaffold, is

sandwiched between the electron and hole transport layers (ETLs and HTLs, respectively). Upon the absorption of incident photons, carriers are created in the absorber that travel through a transport pathway including the ETL or HTL, the electrodes, and each interface in between. To increase the PCE, it is essential to precisely manipulate carriers along the entire pathway from the absorber to both electrodes.

To date, rapid progress has been made on each isolated layer, with major emphasis on perovskite film processing and relevant material design. As a result, various processing approaches have been reported that focus on the absorber properties and consequent device performance (7–15). These include one-step and sequential solution deposition (7–10), vacuum deposition (11), and vapor-assisted solution processing (12), which clearly show a strong relation between the structure, composition, and corresponding properties of the perovskite absorber. Based on a deep understanding of its hybrid nature, a delicate control over the carrier behavior in the perovskite film is expected. Despite our comparatively nascent understanding of this class of absorber

¹Department of Materials Science and Engineering, University of California, Los Angeles, CA 90095, USA. ²California NanoSystems Institute, University of California, Los Angeles, CA 90095, USA.

*These authors contributed equally to this work. †Corresponding author. E-mail: yangy@ucla.edu

materials, much success has been achieved by optimizing the device architecture and introducing new materials as carrier transport layers (16–30), especially ETL materials such as TiO_2 , ZnO , and TiO_2 -graphene composites (20–26). Although the improved electronic properties of these materials could offer device performance advantages, interface barriers between the absorber, transport layer, and electrode are often treated as secondary concerns compared with the generation and preservation of carrier populations in the absorber itself. In pursuit of high PCE, cells will inevitably require an optimized carrier transport pathway that leverages all of the device layers and their corresponding interfaces.

We have manipulated carrier behavior in an efficient carrier pathway across solution-processed planar heterojunction perovskite solar cells through the exploration of the perovskite film, the ETL, and their relevant interfaces. We demonstrate perovskite film deposition through an enhanced reconstruction process in controlled humidity conditions. This process leads to perovskite films with substantially decreased carrier recombination. We also improved the electron transport channel in the device by doping the TiO_2 ETL to enhance its carrier concentration and modifying the ITO electrode to reduce its work function. These changes produced a PCE of 19.3% [see (31) for measurement details]. These findings can be

further used in perovskite-based devices across a variety of applications, such as light-emitting diodes, field-effect transistors, nonlinear optical elements, photoconductive devices, chemical sensors, and radiation detectors.

We fabricated perovskite solar cells with a device architecture similar to the commonly used planar configuration, but with some modifications. The entire device fabrication procedure was carried out at low temperature ($<150^\circ\text{C}$). A scanning electron microscopy (SEM) image of its structure is shown in Fig. 1A. In contrast to the majority of perovskite solar cells, which are based on FTO electrodes, ITO was used as the electrode, which was further modified with polyethyleneimine ethoxylated (PEIE) (32), a polymer containing simple aliphatic amine groups to reduce the work function of ITO. Yttrium-doped TiO_2 (Y-TiO_2) was used as the ETL to enhance electron extraction and transport. For hole extraction, cobalt and lithium co-doped spiro-OMeTAD [2,2',7,7'-tetrakis-(*N,N*-di-4-methoxyphenylamino)-9,9'-spirobifluorene] (8) and gold were used as the HTL and electrode, respectively. The energy levels of relevant functional layers, as determined by ultraviolet (UV) photoelectron spectroscopy (UPS) and UV-visible absorption spectroscopy measurements, are shown in Fig. 1B. With PEIE modification, the work function of ITO was reduced to 4.0 eV from its original 4.6 eV (fig. S1) (31), which facilitates efficient electron transport between the ETL and ITO layers. The Y-TiO_2 layer exhibited a conduction band minimum (CBM) of 4.0 eV (fig. S2) (31). The valence band maximum (VBM) and CBM for the $\text{CH}_3\text{NH}_3\text{PbI}_{3-x}\text{Cl}_x$ are reported as 5.3 and 3.75 eV, respectively (18), and the highest occupied molecular orbital (HOMO) of spiro-OMeTAD was located at 5.22 eV (16). The favorable alignment between the CBM of the Y-TiO_2 and the HOMO of spiro-OMeTAD with the CBM and VBM of the perovskite allows for the efficient extraction of photogenerated carriers without inducing excessive interface recombination or inhibiting quasi-Fermi level splitting within the absorber material.

The characteristics of the perovskite can be optimized during film growth by careful control of the intercalation reaction between the organic and inorganic species. We investigated perovskite film growth under controlled humidity conditions ($30 \pm 5\%$ relative humidity), and we propose an enhanced reconstruction mechanism to explain the observed effects of humidity on device properties. Solution deposition was conducted by directly depositing the mixture of $\text{CH}_3\text{NH}_3\text{I}$ and PbCl_2 (3:1 molar ratio) in a *N,N*-dimethylformamide (DMF) solution onto TiO_2 -coated ITO substrates to fabricate the absorber layer (31).

During annealing under controlled humidity, the film transformed through three distinct stages, as evidenced by x-ray diffraction (XRD) measurements (Fig. 1C) and SEM (Fig. 1, D and E). In the first stage (20 min total annealing time), the film was transparent and light yellow and showed XRD peaks at 7.48° , 12.23° , 14.17° , and 28.51° (Fig. 1C). The peak at 7.48° could not be assigned to any perovskite or lead halide phase

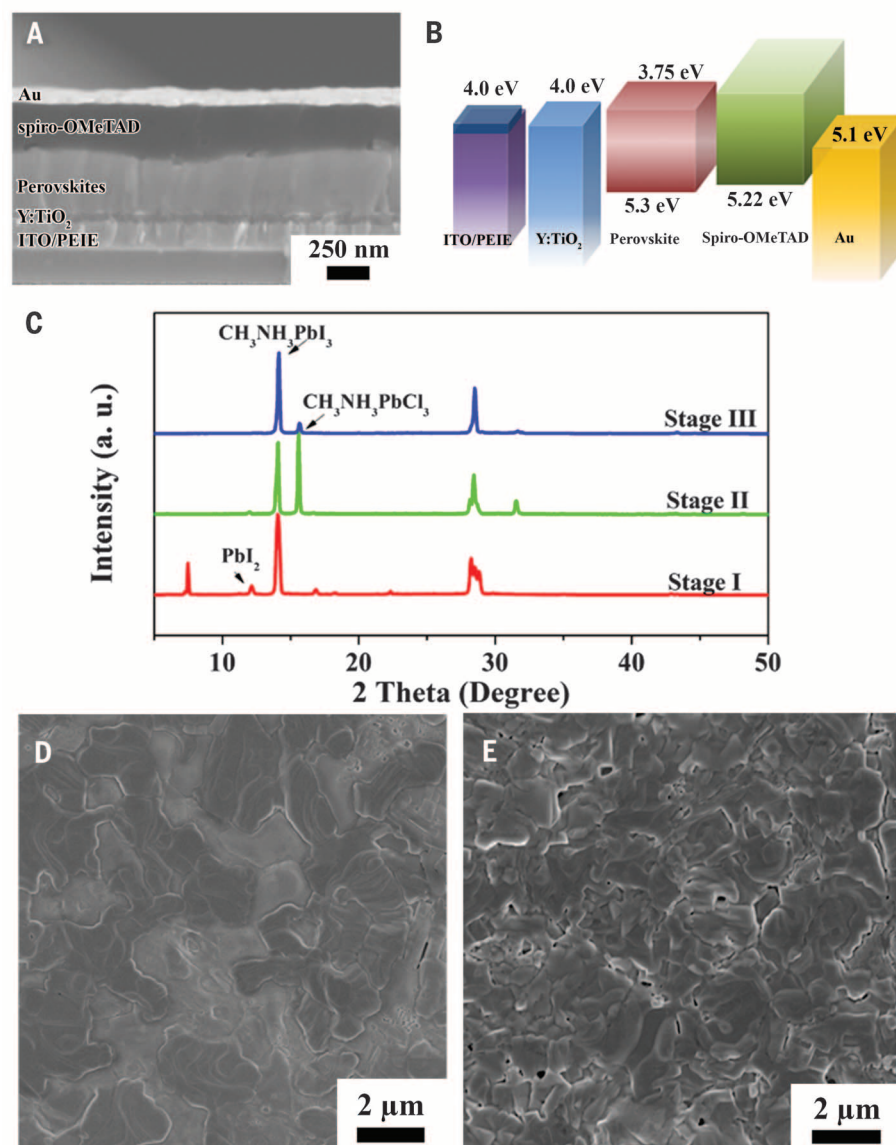


Fig. 1. Structure and energy-level alignment of the perovskite solar cell. (A) SEM cross-sectional image of the device. The layers from the bottom are: (i) ITO/PEIE, (ii) Y-TiO_2 , (iii) perovskite, (iv) spiro-OMeTAD, and (v) Au. (B) Diagram of energy levels (relative to the vacuum level) of each functional layer in the device. (C) XRD patterns corresponding to perovskite film evolution with annealing time (stage I: 20 min, stage II: 60 min, stage III: 85 min). (D and E) Top-view SEM images of perovskite films at stage II (D) and stage III (E).

and is presumably associated with the intermediate of the Pb halide-DMF complex (33). The peak centered at 12.23° was attributed to PbI_2 , and the peaks at 14.17° and 28.51° were assigned to the $\text{CH}_3\text{NH}_3\text{PbI}_3$ phase. The absence of any PbCl_2 phase is possibly a result of ion exchange between Γ^- and Cl^- in the solution or the rapid intercalation reaction that forms the perovskite phase during deposition. In the second stage (60 min total annealing time), the films gradually turned black and opaque and showed two prevalent XRD peaks at 14.17° and 15.57° that we attributed to the $\text{CH}_3\text{NH}_3\text{PbI}_3$ and $\text{CH}_3\text{NH}_3\text{PbCl}_3$ phases, respectively (Fig. 1C). In addition, the intermediate phase (with a peak at 7.48°) disappeared, probably as a result of the removal of residual DMF in the film upon sufficient heating. Excess organic species were likely intercalated into the resulting inorganic framework at this stage of the reaction. At the third stage (85 min total annealing time), the films became dark brown and transparent, and the $\text{CH}_3\text{NH}_3\text{PbCl}_3$ phase observed in the second stage was consumed, leaving $\text{CH}_3\text{NH}_3\text{PbI}_3$ as the dominant phase (Fig. 1C), which is consistent with conversion from $\text{CH}_3\text{NH}_3\text{PbCl}_3$ to $\text{CH}_3\text{NH}_3\text{PbI}_3$ in the presence of excess $\text{CH}_3\text{NH}_3\text{I}$ during film growth. As indicated by previous results (34, 35), the $\text{CH}_3\text{NH}_3\text{PbCl}_3$ phase shows relatively lower thermal stability as compared with $\text{CH}_3\text{NH}_3\text{PbI}_3$. The decomposition of the $\text{CH}_3\text{NH}_3\text{PbCl}_3$ phase may release $\text{CH}_3\text{NH}_3\text{Cl}$ that is replaced by the excess $\text{CH}_3\text{NH}_3\text{I}$ to form $\text{CH}_3\text{NH}_3\text{PbI}_3$ and/or $\text{CH}_3\text{NH}_3\text{PbI}_{3-x}\text{Cl}_x$. The phase transformation described in XRD measurements is in excellent agreement with the SEM images taken at each corresponding stage. Two species with distinct contrast were observed in the film in stage II (Fig. 1D). In stage III (Fig. 1E), the film shows similar contrast and grain size across the entire field of view, which is visibly different from the previous stage.

Without controlled humidity, however, the film-formation process proceeds quite differently. As a reference, films fabricated under dry air conditions were also investigated, and the detailed XRD and SEM characterizations are given in the fig. S5 (37). No strong $\text{CH}_3\text{NH}_3\text{PbCl}_3$ phase was observed at the representative stage, and the final $\text{CH}_3\text{NH}_3\text{PbI}_{3-x}\text{Cl}_x$ film was formed predominantly through the gradual consumption of PbI_2 species. The mechanism of perovskite film formation with moisture involvement is likely to originate from the hygroscopic organic species in the $\text{CH}_3\text{NH}_3\text{PbX}_3$ phases and their nature of ionic crystal. Moisture may enhance the reconstruction process during film formation by partially dissolving the reactant species and accelerating mass transport within the film.

The $\text{CH}_3\text{NH}_3\text{PbI}_{3-x}\text{Cl}_x$ film grown at 30% relative humidity in air exhibited enhanced optoelectronic properties compared with a film grown in dry conditions. We used time-resolved photoluminescence (PL) to characterize radiative and nonradiative carrier recombination of films prepared on glass substrates (Fig. 2A). The PL decay lifetime in the film with enhanced reconstruction

was 736 ns (compared with the reference lifetime of 382 ns), which was likely a result of a reduced defect density that suppressed nonradiative recombination channels.

To further address the carrier behavior in the perovskite and correlate the film properties to device performance, devices with an identical structure were fabricated based on the two films (37). Their corresponding current-voltage (J-V) characteristics (Fig. 2B) show that the reconstruction process increases the perovskite device PCE from 13.5 to 16.4%. Substantial improvement was simultaneously observed in open-circuit voltage from 1.02 to 1.11 V and in fill factor from 61.41 to 65.88%, which together indicate that carrier recombination has been noticeably alleviated in the film with enhanced reconstruction. These findings imply that the optoelectronic properties of perovskite are affected by the phase conversion from $\text{CH}_3\text{NH}_3\text{PbCl}_3$ to $\text{CH}_3\text{NH}_3\text{PbI}_3$ and/or $\text{CH}_3\text{NH}_3\text{PbI}_{3-x}\text{Cl}_x$, and they further emphasize that the halide in the $\text{CH}_3\text{NH}_3\text{PbX}_3$ is vital in determining the material's properties by its close involvement in the film formation.

We further manipulated carrier behavior in the ETL by using Y-TiO₂ to improve the conductivity of this layer. Although TiO₂ is commonly used as the ETL and has appropriate energy levels for transferring electrons while blocking holes, its conductivity is $\sim 1/10$ that of spiro-OMeTAD (36), which may result in unnecessary ohmic losses or a nonideal space charge distribution within the device. To improve the electron transport property, Y-doped TiO₂ has been successfully used as the mesoporous scaffold in dye-sensitized solar

cells and perovskite solar cells; however, it still requires high-temperature sintering (25). Here, Y-TiO₂ nanocrystals processed at low temperature (150°C) were used as the ETL coupled in the planar heterojunction. The J-V characteristics of the solar cells with TiO₂ and Y-TiO₂ as the ETL are shown in Fig. 2C. The TiO₂-based cell produced a short-circuit current (J_{SC}) of $19.9 \text{ mA}/\text{cm}^2$, open-circuit voltage (V_{OC}) of 1.06 V, and fill factor (FF) of 65.44%, yielding a PCE of 13.8%, whereas the Y-TiO₂-based device had J_{SC} of $22.8 \text{ mA}/\text{cm}^2$ and a PCE of 16.5%. There was no apparent difference between the absorbance of perovskite films deposited on the two substrates. Four-point conductivity measurements revealed a higher conductivity ($2 \times 10^{-5} \text{ S}/\text{cm}$) for the Y-TiO₂ film versus the undoped TiO₂ film ($6 \times 10^{-6} \text{ S}/\text{cm}$), possibly due to the increased carrier concentration. The series resistance in the device was also reduced from 9.12 to 5.34 ohms. The improved conductivity of Y-TiO₂ matches that of spiro-OMeTAD (26), which balances the carrier transport to reduce nonideal space charge distribution.

A Schottky barrier at the interface between TiO₂ and the transparent conductor can cause an apparent decrease in the maximum power output when it becomes too large (37). The general principle to reduce the interfacial barrier at a metal-semiconductor junction on the n-type side of a device is to reduce the work function of the metal being used. Modification of the electrode to achieve a work function that is near or lower than the Fermi energy of TiO₂ will then facilitate electron collection at the interface. Here, a solution of PEIE in methoxyethanol ($\sim 0.1\%$ by weight)

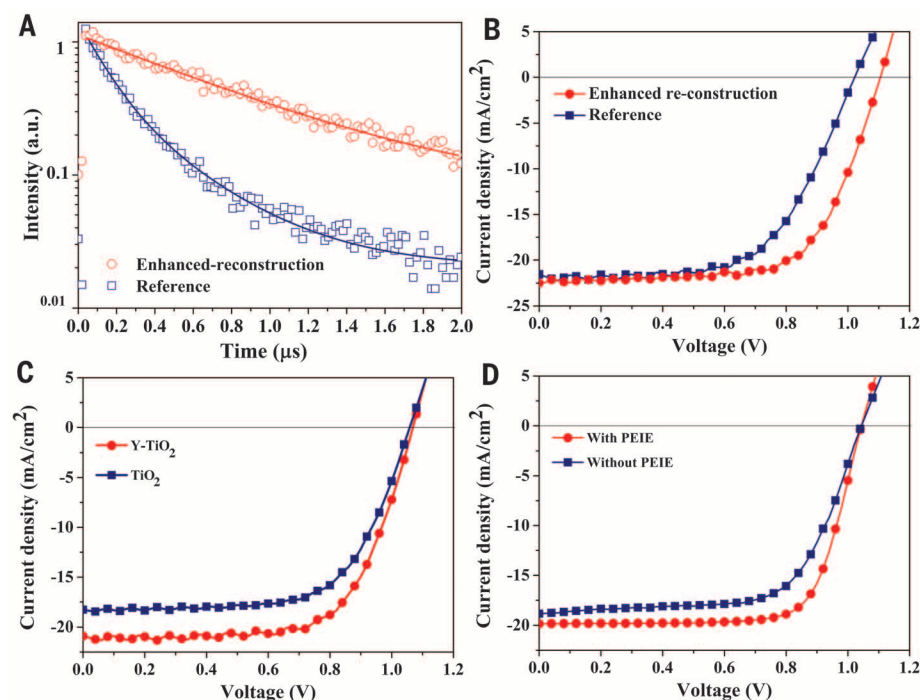


Fig. 2. Photoluminescence and photovoltaic characterization. (A) Photoluminescence decay curves of perovskite films prepared in controlled humidity (red circles) and dry air (blue squares). a.u., arbitrary units. (B) J-V curves of devices based on the corresponding films. (C) J-V curves of devices with Y-TiO₂ compared with undoped TiO₂. (D) J-V curves of devices with and without PEIE modification.

was used to form an ultrathin layer physisorbed on the ITO surface. The introduced molecular dipole interactions successfully reduced the work

function of ITO from 4.6 to 4.0 eV. This shift likely helped to facilitate improved electron transport from the TiO₂ to ITO layers. As shown in Fig.

2D, an increase of fill factor in the PEIE-modified device was observed, which is consistent with the suppression of a barrier to carrier injection into the electrode. PEIE modification enables a perovskite solar cell with PCE >15%, in which $V_{OC} = 1.04$ V, $J_{SC} = 19.9$ mA/cm², and FF = 73.28%. As a comparison, the device without PEIE modification exhibited $V_{OC} = 1.04$ V, $J_{SC} = 18.9$ mA/cm², and FF = 65.25%. In addition, we observed a slightly reduced surface roughness of the perovskite films with relevant morphology change due to the employment of PEIE on the ITO substrates (fig. S6) (31).

Combined optimization of the entire carrier pathway has led to a device PCE of 19.3% under AM1.5 illumination without antireflective coating; the V_{OC} , J_{SC} , and FF are 1.13 V, 22.75 mA/cm², and 75.01%, respectively (Fig. 3). The error in J_{SC} measurement is within 5% by considering that light intensity, spectrum mismatch, and testing mask aperture effect (31). In general, the devices exhibit $V_{OC} = 1.04$ to 1.15 V, $J_{SC} = 18.16$ to 22.80 mA/cm², FF = 66.9 to 76.3%, and the resulting PCE = 14.5 to 19.3%. The average device efficiency is more than 16.6%, which shows the good reproducibility of the approach. The external quantum efficiency (EQE) spectrum (Fig. 3C) of a typical device (in-house measured V_{OC} , J_{SC} , FF, and PCE are 1.08 V, 21.26 mA/cm², 75.36%, and 17.3%, respectively, under AM1.5G, as shown in the inset of Fig. 3C) shows the onset of photocurrent at 790 nm, consistent with the reported band gap of CH₃NH₃PbI_{3-x}Cl_x (18). The EQE reaches a peak value at ~550 nm with a gradual decrease from 600 nm, indicating a photocurrent loss due to either insufficiency in the absorption of perovskite layer or optical interference. The use of a simple planar structure and the production of such high-efficiency devices with low-temperature processing confirm the extraordinary potential of perovskite materials in photovoltaic applications. The representative device shows hysteresis in the current-voltage curves (fig. S8) (31), which is similar to the findings of a recent report (38). We also carried out a preliminary stability investigation of the perovskite solar cell by storing the devices in different environments. As shown in fig. S9 (31), the devices stored in either dry air or nitrogen retain 80% of the initial performance after 24 hours and 20% after 6 days, whereas the devices stored in ambient air retain less than 20% of the initial performance after 24 hours and 5% after 6 days. These results show that better stability with advanced encapsulation techniques is needed for practical use of the perovskite solar cells.

To further examine the origin of the improved device characteristics, we used transient photovoltage and photocurrent measurements to investigate the carrier dynamics along the entire pathway in the completed cells. Transient photovoltage measurements, which correlate to the electron lifetime in the absorber, provide insight into carrier recombination rates in the cell. Two devices were compared: one was based on a perovskite film with enhanced reconstruction ($V_{OC} = 1.13$ V, $J_{SC} = 22.06$ mA/cm², FF = 71.25%,

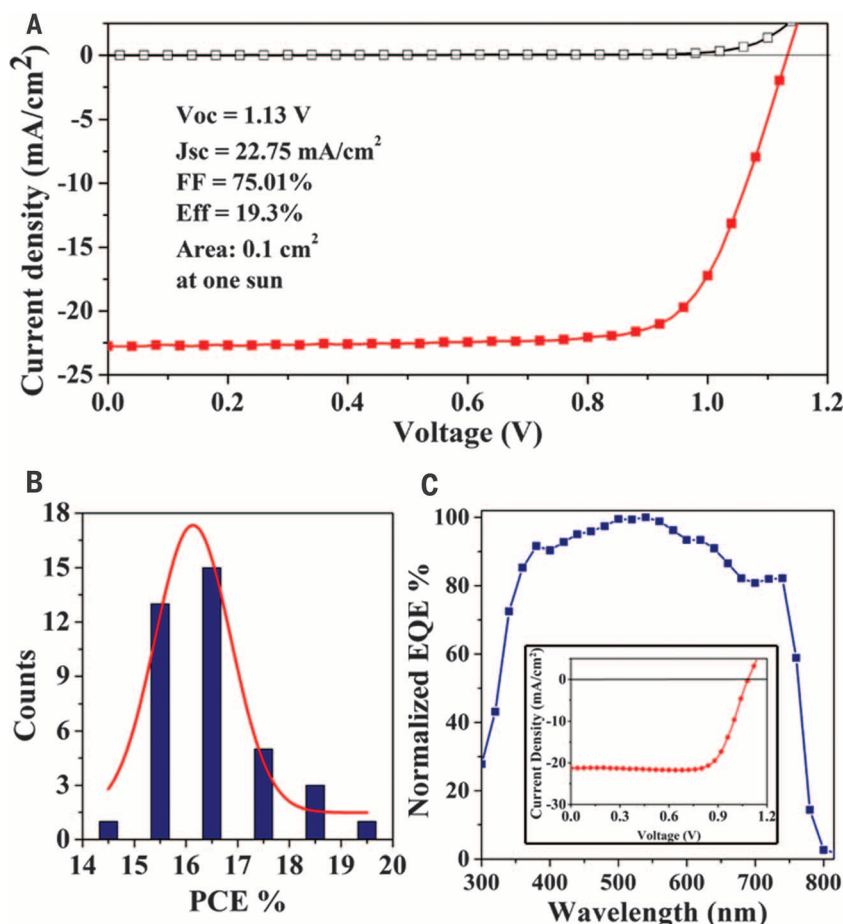
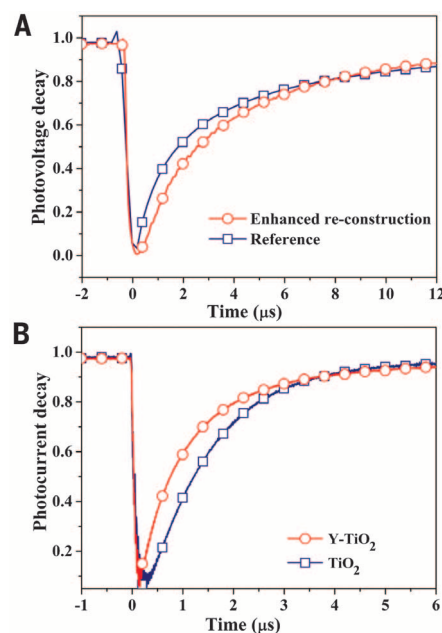


Fig. 3. Efficiency measurements. (A) J-V curves for the champion cell without antireflective coating. (B) Histogram of solar cell efficiencies for 40 devices. (C) Normalized EQE spectrum of a typical cell. (Inset) The corresponding J-V curve of the device.

Fig. 4. Carrier lifetimes. (A) Transient photovoltage decay curves of devices with perovskite absorbers processed in controlled humidity (red circles) and in dry air (blue squares). (B) Transient photocurrent decay curves of devices based on ETL of TiO₂ (blue squares) and Y-TiO₂ (red circles).



PCE = 17.76%), and the other was the reference without enhanced reconstruction ($V_{OC} = 1.02$ V, $J_{SC} = 20.53$ mA/cm², FF = 61.41%, PCE = 12.85%). Based on the voltage decay time, the device with the enhanced reconstruction film showed ~50% longer electron lifetime than that of the reference cell (Fig. 4A). In both cases, the photovoltage decay constants are on the scale of microseconds. This is consistent with the observation of very slow microsecond time scale recombination at ambient solar intensities (39), indicating that the carrier recombination is predominately limited by the perovskites layer. This result also reveals that the photovoltage decay time benefits from substantially reduced trap densities in the perovskite material or at its interfaces by enhanced reconstruction film formation. This observation is in good agreement with both the longer carrier lifetime, as mentioned previously, and the decreased saturation current density (fig. S10) (37). Note that high V_{OC} value reported here is near the thermodynamic limit, which is constrained by radiative recombination in the absorber (40).

Transient photocurrent measurements indicate that carrier transport in the devices was improved by modification in the TiO₂ layer. The Y-TiO₂-based devices exhibited faster photocurrent decay than that of reference devices, in which the perovskite layers were deposited by the same method. This result is in accordance with the PL measurements (fig. S11) (37), where perovskites on Y-TiO₂ layer showed a decay time ~30% smaller than the reference. More efficient carrier extraction in the Y-TiO₂ devices probably resulted from the improved interface at the Y-TiO₂ layer. UPS characterization exhibited a slight upward shift of the Fermi level in the Y-TiO₂ layer, indicating an increased donor concentration in response to the enhanced conductivity. This is further confirmed by the capacitance-voltage measurement (fig. S12) (37). Increased donor concentration often reduces space charge depletion width at interfaces (26). Presumably, the narrower depletion region lowers the contact resistance and facilitates the charge extraction at both interfaces adjacent to the ETL.

REFERENCES AND NOTES

1. D. B. Mitzi, *Prog. Inorg. Chem.* **48**, 1–121 (2007).
2. A. Kojima, K. Teshima, Y. Shirai, T. Miyasaka, *J. Am. Chem. Soc.* **131**, 6050–6051 (2009).
3. www.nrel.gov/ncpv/images/efficiency_chart.jpg.
4. B. V. Lotsch, *Angew. Chem. Int. Ed.* **53**, 635–637 (2014).
5. N.-G. Park, *J. Phys. Chem. Lett.* **4**, 2423–2429 (2013).
6. H. J. Snaith, *J. Phys. Chem. Lett.* **4**, 3623–3630 (2013).
7. M. M. Lee, J. Teuscher, T. Miyasaka, T. N. Murakami, H. J. Snaith, *Science* **338**, 643–647 (2012).
8. J. Burschka et al., *Nature* **499**, 316–319 (2013).
9. J.-Y. Jeng et al., *Adv. Mater.* **25**, 3727–3732 (2013).
10. D. Liu, T. L. Kelly, *Nat. Photonics* **8**, 133–138 (2014).
11. M. Liu, M. B. Johnston, H. J. Snaith, *Nature* **501**, 395–398 (2013).
12. Q. Chen et al., *J. Am. Chem. Soc.* **136**, 622–625 (2014).
13. G. E. Eperon, V. M. Burlakov, P. Docampo, A. Goriely, H. J. Snaith, *Adv. Funct. Mater.* **24**, 151–157 (2014).
14. B. Conings et al., *Adv. Mater.* **26**, 2041–2046 (2014).
15. P.-W. Liang et al., *Adv. Mater.* **26**, 3748–3754 (2014).
16. H. S. Kim et al., *Sci. Rep.* **2**, 591 (2012).
17. O. Malinkiewicz et al., *Nat. Photonics* **8**, 128–132 (2014).
18. P. Docampo, J. M. Ball, M. Darwich, G. E. Eperon, H. J. Snaith, *Nat. Commun.* **4**, 2761 (2013).
19. J. H. Heo et al., *Nat. Photonics* **7**, 486–491 (2013).

20. A. Abruci et al., *Nano Lett.* **13**, 3124–3128 (2013).
21. H.-S. Kim et al., *Nano Lett.* **13**, 2412–2417 (2013).
22. A. Yella, L.-P. Heiniger, P. Gao, M. K. Nazeeruddin, M. Grätzel, *Nano Lett.* **14**, 2591–2596 (2014).
23. Z. Zhu et al., *J. Am. Chem. Soc.* **136**, 3760–3763 (2014).
24. D.-Y. Son, J.-H. Im, H.-S. Kim, N.-G. Park, *J. Phys. Chem. C* (2014).
25. P. Qin et al., *Nanoscale* **6**, 1508–1514 (2014).
26. K. Wojciechowski, M. Saliba, T. Leijtens, A. Abate, H. Snaith, *Energy Environ. Sci.* **7**, 1142–1147 (2014).
27. J. A. Christians, R. C. M. Fung, P. V. Kamat, *J. Am. Chem. Soc.* **136**, 758–764 (2014).
28. N. J. Jeon et al., *J. Am. Chem. Soc.* **135**, 19087–19090 (2013).
29. J. You et al., *ACS Nano* **8**, 1674–1680 (2014).
30. W. Zhang et al., *Nano Lett.* **13**, 4505–4510 (2013).
31. See supplementary materials on Science Online.
32. Y. Zhou et al., *Science* **336**, 327–332 (2012).
33. I. Persson, K. Lyczko, D. Lundberg, L. Eriksson, A. Placzek, *Inorg. Chem.* **50**, 1058–1072 (2011).
34. J. Błazejowski, E. Kowalewska, *Thermochim. Acta* **105**, 257–286 (1986).
35. P. Dokurno, J. Łubkowski, J. Błazejowski, *Thermochim. Acta* **165**, 31–48 (1990).
36. T. Leijtens, J. Lim, J. Teuscher, T. Park, H. J. Snaith, *Adv. Mater.* **25**, 3227–3233 (2013).
37. H. J. Snaith, M. Grätzel, *Adv. Mater.* **18**, 1910–1914 (2006).
38. H. J. Snaith et al., *J. Phys. Chem. Lett.* **5**, 1511–1515 (2014).
39. C. S. Ponceca Jr. et al., *J. Am. Chem. Soc.* **136**, 5189–5192 (2014).

40. R. R. King et al., *Prog. Photovolt. Res. Appl.* **19**, 797–812 (2011).

ACKNOWLEDGMENTS

This work was financially supported by a grant from the NSF (grant no. ECCS-1202231, Program Director P. Werbos), a grant from the Air Force Office of Scientific Research (grant no. FA9550-12-1-0074, Program Manager C. Lee), and UCLA Internal Funds. We thank H. S. Jung and B. Kim of Sungkyunkwan University in Korea for valuable discussion in the starting stage of a perovskite solar cell, S. Lu for synthesizing Co salt, B. Bob and E. Richard for editing, W. Hsu for assistance with UPS measurements and analysis, L. Dou for TiO₂ nanocrystal synthesis, J. D. Huang for inspiring technical discussion, K. Emery (National Renewable Energy Laboratory) for calibrating UCLA's in-house KG5 Si reference cell and valuable discussion on EQE measurement, and M. O'Donnell (Newport Corporation) for helping on spectral mismatch factor calculation.

SUPPLEMENTARY MATERIALS

www.sciencemag.org/content/345/6196/542/suppl/DC1
Materials and Methods
Figs. S1 to S12
Tables S1 and S2
Reference (41)

28 March 2014; accepted 18 June 2014
10.1126/science.1254050

CATALYSIS

Highly active copper-ceria and copper-ceria-titania catalysts for methanol synthesis from CO₂

Jesús Graciani,¹ Kumudu Mudiyanse, ² Fang Xu,² Ashleigh E. Baber,² Jaime Evans,³ Sanjaya D. Senanayake,² Darío J. Stacchiola,² Ping Liu,² Jan Hrbek,² Javier Fernández Sanz,¹ José A. Rodríguez^{2*}

The transformation of CO₂ into alcohols or other hydrocarbon compounds is challenging because of the difficulties associated with the chemical activation of CO₂ by heterogeneous catalysts. Pure metals and bimetallic systems used for this task usually have low catalytic activity. Here we present experimental and theoretical evidence for a completely different type of site for CO₂ activation: a copper-ceria interface that is highly efficient for the synthesis of methanol. The combination of metal and oxide sites in the copper-ceria interface affords complementary chemical properties that lead to special reaction pathways for the CO₂→CH₃OH conversion.

Methanol is a key commodity used to produce acetic acid, formaldehyde, and a number of key chemical intermediates (1). It is synthesized industrially from mixtures of H₂, CO₂, and CO at elevated pressures (50 to 100 atm) and temperatures (450 to 600 K) with a Cu/ZnO/Al₂O₃ catalyst (2–4). Of particular interest is the synthesis of methanol from CO₂ (2, 5–9), not only as a way to mitigate this greenhouse gas but also because of the potential use of CO₂ as an alternative and

economical feedstock (2, 5, 10–12). The activation of CO₂ and its hydrogenation to alcohols or other hydrocarbon compounds is an important approach to recycle the released CO₂ (2, 5, 11, 12). This is a challenging task because of the difficulties associated with the chemical inertness of CO₂ (2, 5–9, 13). A recent study has identified the active site for the activation of CO₂ and the synthesis of methanol on Cu/ZnO/Al₂O₃ industrial catalysts (2). The active site consists of Cu steps decorated with Zn atoms. Cu alone interacts very poorly with CO₂ (2, 6–9), and alloying with Zn is necessary in order to bind the reactant better and accelerate its transformation into methanol (2). Here we present experimental and theoretical evidence for a completely different type of site for CO₂ activation: A Cu-ceria interface, which is highly active for the synthesis of

¹Department of Physical Chemistry, University of Seville, E-41012, Seville, Spain. ²Department of Chemistry, Brookhaven National Laboratory, Upton, NY 11973, USA. ³Facultad de Ciencias, Universidad Central de Venezuela, Caracas, 1020-1, Venezuela.

*Corresponding author. E-mail: rodriguez@bnl.gov



Interface engineering of highly efficient perovskite solar cells

Huanping Zhou *et al.*

Science **345**, 542 (2014);

DOI: 10.1126/science.1254050

This copy is for your personal, non-commercial use only.

If you wish to distribute this article to others, you can order high-quality copies for your colleagues, clients, or customers by [clicking here](#).

Permission to republish or repurpose articles or portions of articles can be obtained by following the guidelines [here](#).

The following resources related to this article are available online at www.sciencemag.org (this information is current as of March 14, 2016):

Updated information and services, including high-resolution figures, can be found in the online version of this article at:

</content/345/6196/542.full.html>

Supporting Online Material can be found at:

</content/suppl/2014/07/30/345.6196.542.DC1.html>

This article **cites 39 articles**, 2 of which can be accessed free:

</content/345/6196/542.full.html#ref-list-1>

This article has been **cited by** 10 articles hosted by HighWire Press; see:

</content/345/6196/542.full.html#related-urls>

This article appears in the following **subject collections**:

Physics, Applied

/cgi/collection/app_physics